RESEARCH ARTICLE

Energy & Environmental Materials WILEY

Electrolytes

Charting Water-in-Natural-Salt (WiNS) Electrolytes. Part I: Effect of Anion's Alkyl Tail Length

Alessandra Del Giudice, Laura Hildebrandt, Jin Han, Radhika Krishna Hema, Luciano Galantini, Stefano Passerini, Alberto Varzi, and Alessandro Mariani**

Water-in-natural-salt electrolytes are fluorine-free candidates for safer high voltage aqueous energy storage. We study 20 m solutions of potassium formate, acetate, propionate, and butyrate to test how anion amphiphilicity controls nanostructure, ion transport, and electrochemical stability. Small-angle X-ray scattering reveals a low-*q* pre-peak that shifts to lower *q* with increasing tail length, consistent with a growing modulation length and a distorted sponge-like bicontinuous morphology. Molecular dynamics assigns this pre-peak to concentration–concentration fluctuations that co-localize water and K^+ in polar channels, anticorrelated with anion-centered alkyl domains. Water cluster analysis shows that average cluster size drops from formate to acetate in parallel with a pronounced widening of the electrochemical stability window, while conductivity decreases along the series. These trends identify potassium acetate as an optimal compromise between stability and mobility and suggest structural targets for fluorine-free aqueous electrolytes.

1. Introduction

Lithium-ion batteries remain the benchmark for electrochemical energy storage, yet the organic electrolytes that enable high energy density also impose safety, volatility, and cost penalties at system scale.[1–3] As electrification spreads across mobility, grid, and industrial settings, the electrolyte brief has broadened: Platforms must deliver acceptable performance while remaining intrinsically safe, supply-robust, and simple to manufacture and recycle.[4–7] This has reinvigorated interest in aqueous electrolytes, where water's benign handling contrasts with its reactivity constraining the voltage window and limiting compatibility with many electrode chemistries.[8–13]

Water-in-salt electrolytes (WiSE) reframed this landscape by using extreme salt content to depress water activity and reorder local solvation, thereby mitigating parasitic reactions and expanding the apparent aqueous stability window.[13] In such solutions, the electrolyte behaves less like "salt in water" and more like a crowded, ion-rich fluid in which water plays a structural and dynamic co-solvent role.[14–17] This concentration regime shifts transport, structure, and interfacial kinetics in ways that are not captured by dilute-solution intuitions and demands characterization strategies that emphasize robust observables and careful cross-system comparisons.[15,18–26]

However, many WiSE exemplars rely on fluorinated anions whose cost, environmental footprint, and end-of-life handling run counter to the sustainability motivations that make aqueous platforms attractive.[17] This has spurred the search for fluorine-free formulations that maintain low water activity and favorable interfacial behavior while leveraging commodity feedstocks and simpler decomposition profiles.[21,23,25] A promising path is to exploit amphiphilicity, embedding apolar moieties into otherwise hydrophilic salts, so that medium-range organization emerges without introducing fluorine, potentially reproducing beneficial aspects of WiSE structure–property relationships at lower material complexity.[27–29] In concentrated electrolytes, this organization is not crystalline or lamellar; rather, it manifests as mesoscale concentration fluctuations that affect transport pathways and interfacial response.[27–29]

Small-and-wide-angle X-ray scattering (SWAXS) is sensitive to such medium-range organization. In numerous ionic liquids, concentrated electrolytes, and amphiphilic salts, a low-q maximum ("pre-peak") signals composition modulation between polar and apolar microenvironments and is dominated by the concentration–concentration Bhatia–Thornton (BT) channel, not by long-range order.[30–33] Details on the theoretical background can be found in the Supporting Information.

Here we examine fluorine-free, water-in-natural-salt (WiNS) electrolytes formed by a homologous series of potassium carboxylates: formate (C_1OOK), acetate (C_2OOK), propionate (C_3OOK), and butyrate

Dr. A. Del Giudice, Prof. L. Galantini
Dipartimento di Chimica, Sapienza Università di Roma, piazzale Aldo Moro 5, 00185, Rome, Italy
L. Hildebrandt, Prof. J. Han, R. K. Hema, Prof. S. Passerini, Dr. A. Varzi, Dr. A. Mariani
Helmholtz Institute Ulm (HIU), Helmholtzstrasse 11, 89081, Ulm, Germany
Karlsruhe Institute of Technology (KIT), P.O. Box 3640, 76021, Karlsruhe, Germany
E-mail: alberto.varzi@kit.edu
E-mail: alessandro1.mariani@polimi.it
Prof. J. Han
International School of Materials Science and Engineering, School of Materials Science and Microelectronics, Wuhan University of Technology, Wuhan 430070, China
Prof. S. Passerini
Austrian Institute of Technology (AIT), Center of Transport Technologies (TT), Giefinggasse 2, 1210, Vienna, Austria
Dr. A. Mariani
Dipartimento di Chimica, Materiali e Ingegneria Chimica "Giulio Natta", Politecnico di Milano, via Bassini 6, 20131, Milan, Italy
The ORCID identification number(s) for the author(s) of this article can be found under https://doi.org/10.1002/eem2.70359.

DOI: 10.1002/eem2.70359

(C_4OOK). The selection of Potassium is dictated by the very large solubility of its carboxylate salts when compared to the Lithium and Sodium counterparts. Thus, while the applicability of such electrolytes in actual batteries could be difficult, the study aims at catching general trends that can help in understanding the physical and chemical behavior of these highly concentrated solutions. Studying a single composition across the series ensures a like-for-like comparison in which the alkyl tail is the principal tuned variable, while keeping the cation and overall salt motif constant.[27–29] Our central hypothesis is that increasing tail length coarsens the modulation length (larger d, lower $q_{pre\text{-}peak}$) and modestly narrows the distribution of domain sizes (smaller width, larger coherence), thereby strengthening mesoscale segregation between polar and apolar regions. We further hypothesize that this structural tuning links to function in two ways: 1) by shaping pathways that govern interfacial reaction onset, thus influencing the electrochemical stability window, and 2) by altering the temperature dependence of ion transport as captured by Vogel–Tammann–Fulcher (VTF) analyses.[19,34,35] To test these ideas, we combine SAXS with molecular dynamics (MD) and experimental electrochemistry.

In this work, we first establish the SWAXS signatures across C_1OOK–C_4OOK, emphasizing pre-peak position and width and clarifying the limits of what those observables can claim. We then use MD and BT analysis to attribute the pre-peak to specific partial channels and to visualize the associated concentration modulation. Finally, we connect these structural trends to the electrochemical stability window and to temperature-dependent conductivity within the VTF framework, highlighting where correlations are strong and where interfacial specifics likely decouple bulk structure from onset behavior.

2. Results and Discussion

Figure 1 compiles the SWAXS patterns at 20 m for C_1OOK, C_2OOK, C_3OOK, and C_4OOK, and **Table 1** reports the corresponding $q_{pre\text{-}peak}$ and modulation lengths $d = 2\pi/q_{pre\text{-}peak}$. Each WiNS sample shows a system-dependent maximum at $q < 1$ Å^{-1} together with a weaker feature near $q \approx 1.5$ Å^{-1}.

To isolate structural trends from contrast differences, we compare peak positions of WiNS against neat n-alkyl carboxylic acids,[28] 20 m aqueous n-alkyl carboxylic acids solutions (curves in Figure S1, Supporting Information), linear mono-ols,[29,36] and ionic systems such as alkylammonium nitrates that show similar chain length-dependent low-q features.[27,37–39] Within the 20 m C_xOOK series, pseudo-Voigt fitting yields $q_{pre\text{-}peak}$ values that decrease monotonically from C_1OOK to C_4OOK, so d increases with tail length (Figure 1c, Table 1). Full widths at half maximum narrow with increasing the alkyl tail, which indicates a modest increase in the coherence length of the modulation distance (Figure 1a inset).

Because resolution deconvolution is not applied, these widths are apparent and are interpreted only within the same setup.[41,42] Parameters and confidence intervals are reported in Table S2, Supporting Information. A linear fit of d versus the number of methylene units returns a slope of about 3 Å per CH (Figure 1c), much larger than the Tanford chain-extension increment for neutral amphiphiles, approximately 1.27 Å per CH.[43,44] This difference is reasonable for concentrated electrolytes, where solvated ions and extended polar networks can enlarge the effective correlation length at the same tail length. The left shift of the pre-peak with increasing chain length seen here is consistent with trends in all the series in Table 1. C_1OOK is an edge case: At 20 m, it shows a broad maximum near $q \sim 1.0$ Å^{-1}; for such wide features, the pseudo-Voigt mixing parameter is known to be not physically meaningful,[42] but the other parameters stay valid. We also analyzed the azimuthally averaged SWAXS curves with the Teubner–Strey (TS) expression,[45,46] which parameterizes the line shape through a quasi-periodic spacing d and a correlation length ξ, fitted together with a flat background and a scale factor (fittings in Figure S2, Supporting Information). The d values are seen to increase systematically with alkyl chain length, while ξ also grows, and the ξ/d ratio rises across the series, as shown in Table S3, Supporting Information. This behavior mirrors the simple pseudo-Voigt analysis, where the pre-peak position shifts to lower q and the width narrows along the same sequence, which is consistent with larger d and larger ξ in the TS model. Figure 1d plots ξ/d versus tail length to summarize damping of the concentration modulation in a scale independent way. Values above unity indicate an underdamped regime in which the correlations persist over more than one repeating unit distance, which produces a relatively sharp low-q maximum, while ratios clearly below unity correspond to more strongly damped fluctuations, which broaden the pre-peak. Near unity marks the crossover between underdamped and overdamped behavior.[45,46] The ratio is model-based and does not by itself prove a specific topology, although values greater than one are commonly reported for systems that exhibit extended concentration modulations in small-angle scattering. Morphological labels are not assigned at this stage, as will be discussed in the next section. Within our q-range, we do

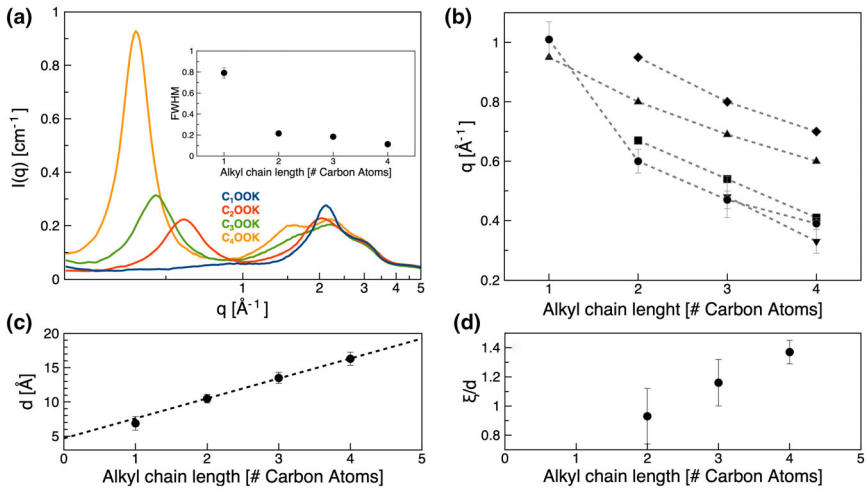

Figure 1. a) SWAXS profiles of 20 m potassium carboxylates in water at room temperature: C_1OOK (blue), C_2OOK (red), C_3OOK (green), C_4OOK (orange). Inset: FWHM of the pre-peaks obtained by pseudo-Voigt fitting. b) $q_{pre\text{-}peak}$ versus carbon number for 20 m potassium carboxylates in water (circles), 20 m aqueous carboxylic acids (inverted triangles), n-alkylammonium nitrates (squares), linear alcohols (triangles), and neat carboxylic acids (diamonds). Lines are guides to the eye. c) Linear fitting of the characteristic distance d as a function of carbon atoms in the alkyl tail, parameters in Table S4, Supporting Information. d) Teubner–Strey fitting derived ξ/d ratio.

Table 1. Low-q pre-peak positions from SWAXS for different liquid classes versus the carbons' number in the alkyl tail. Values in $Å^{-1}$, corresponding real-space lengths $d = 2\pi/q$ are given in parentheses (Å).

Family	C_1	C_2	C_3	C_4
20 m potassium n-carboxylate in water (water-in-natural-salt)	1.01 ± 0.06 (6.22 ± 0.37)	0.60 ± 0.04 (10.47 ± 0.70)	0.47 ± 0.03 (13.37 ± 0.85)	0.39 ± 0.02 (16.11 ± 0.83)
n-Alcohol (molecular liquid)	0.95[29] (6.61)	0.80[29] (7.85)	0.69[29] (9.10)	0.60[29] (10.47)
n-Carboxylic acid (molecular liquid)	None[28]	0.93[28] (6.67)	0.80[28] (7.85)	0.69[28] (9.11)
n-Alkylammonium nitrate (ionic liquid)	None[40]	0.67[38] (9.38)	0.53[38] (11.86)	0.44[38] (14.28)
20 m n-carboxylic acid in water (molecular mixture)	None	None	0.48 ± 0.07 (13.09 ± 1.91)	0.33 ± 0.04 (19.04 ± 2.31)

not observe a harmonic at $2 \cdot q_{pre\text{-}peak}$. Taken together with the left shift and narrowing of the peak, these observations do not motivate invoking layered periodicity. A mid-q shoulder appears near $q \approx 1.5$ $Å^{-1}$ from propionate to butyrate. The associated real-space scale, 4.2 Å, is commonly linked in the literature to local charge-alternation correlations; here, we record its coexistence with the low-q maximum and its strengthening with increasing chain length, deferring explicit channel-level assignment to the MD analysis that follows. In summary, concentrated aqueous benchmarks support treating the pre-peak position as a readout of a composition-modulation length in macroscopically homogeneous liquids. In water-in-salt systems, a small-angle pre-peak tracks a mesoscale modulation in both scattering and simulation, with detailed mechanistic assignment provided by the MD section.

3. Molecular Dynamics

The molecular dynamics analysis assigns the SWAXS observables to specific correlation channels and thereby provides a model-based morphology. The models have been validated through density check (Table S1, Supporting Information) and by comparing the experimentally derived[47] and calculated S(q) (Figure S3, Supporting Information). We rely on species-resolved partial structure factors and on the BT decomposition into number–number, concentration–concentration, and charge–charge channels, which together reconstruct the total structure factor measured by scattering.[48] For clarity, we refer to the working relations given as Equations (1–3), which link I(q) (scattered intensity) to the simulated S(q) (structure factor) and to the $S_{ij}(q)$ (partial structure factor) that identify pairs of species carrying each feature:[42,48–50]

$$S(q) = \frac{I(q)}{\sum_i \chi_i \cdot f_i^2} - 1, \tag{1}$$

$$S(q) = 4\pi \sum_{i,j} \rho_{i,j} \int_0^{r_{max}} r^2 \left(g_{i,j}(r) - 1\right) \frac{\sin(qr)}{qr}\, dr, \tag{2}$$

$$S(q) = \sum_{i,j} S_{i,j}(q). \tag{3}$$

A central diagnostic advantage of partial structure factors is their sign freedom. Negative features are allowed and expected when channels are anticorrelated and the sum rule is preserved. In practice, an anti-peak in $S_{ij}(q)$ implies a real-space deficit of i around j on the distance scale set by that q, whereas a positive feature reflects preferred co-location. This property enables a direct readout of which correlations underpin the experimental pre-peak without relying on amplitude comparisons across unrelated chemistries.[49,51] **Figure 2** gathers the MD observables.

The low-q maximum observed by SWAXS is carried in the simulations primarily by the concentration–concentration sector of the BT decomposition. In the species view (Figure 2b), water–K^+ and like-polarity terms (Figure 2c) contribute positively at $q \approx q_{pre\text{-}peak}$, while cross-polarity terms contribute negative weight at the same q, consistent with a modulation of polar and apolar environments on the length scale $d = 2\pi/q_{pre\text{-}peak}$. This sign structure is the expected fingerprint of polarity-segregated fluctuations in dense ionic media and is widely used to rationalize the low-q feature in ionic liquids when alkyl tails grow in length.[49] The pronounced positive feature in $S_{K^+-K^+}(q)$ at the pre-peak position directly reflects the presence of K^+-rich domains separated by the characteristic modulation length. Conversely, the negative weight of $S_{Anion-K^+}(q)$ over the same low-q range shows that carboxylate anions are depleted from those K^+-rich regions at that length scale and preferentially occupy the complementary domains. The BT pattern of positive like-polarity and negative cross-polarity contributions at the pre-peak is therefore the reciprocal-space fingerprint of polar (K^+ plus water) domains anticorrelated with alkyl-rich domains. This BT pattern can be viewed within the sol–gel framework proposed for water-in-salt electrolytes.[52] In that picture, a percolating ionic gel of space spanning charged domains coexists with a more mobile sol comprising neutral or weakly charged species. For C_2OOK–C_4OOK, the positive concentration–concentration weight of the K^+ plus water channel at $q_{pre\text{-}peak}$, together with the percolation analysis of the trajectories, identifies the K^+ rich polar network as the ionic gel, while the alkyl-rich regions and more weakly bound water form the complementary sol phase. The model therefore explains the experimental left-shift of $q_{pre\text{-}peak\ from\ C2}$OOK to C_4OOK as the reciprocal-space signature of an increasing modulation length carried by concentration–concentration fluctuations, and it also accounts for the peak narrowing observed, as all the radial distribution functions in Figure 2d increase in intensity with longer alkyl tails, hinting at a higher probability of the corresponding correlation. C_1OOK behaves differently and matches the experimental edge case. The simulated low-q enhancement appears at higher q and is broader than for the longer-tail salts, mirroring the SWAXS trend. In the BT grouping, the in-phase like-polarity rise plus cross-polarity anti-peak that characterizes C_2OOK–C_4OOK is not present in C_1OOK. Instead, correlations in the low-q window are dominated by hydration-centric structure where water and ions co-organize without forming a persistent apolar counterpart at the corresponding length scale (panels H_2O-H_2O and H_2O-K^+ in Figure 2b).[53–55] This channel-level behavior explains why C_1OOK sits at the boundary

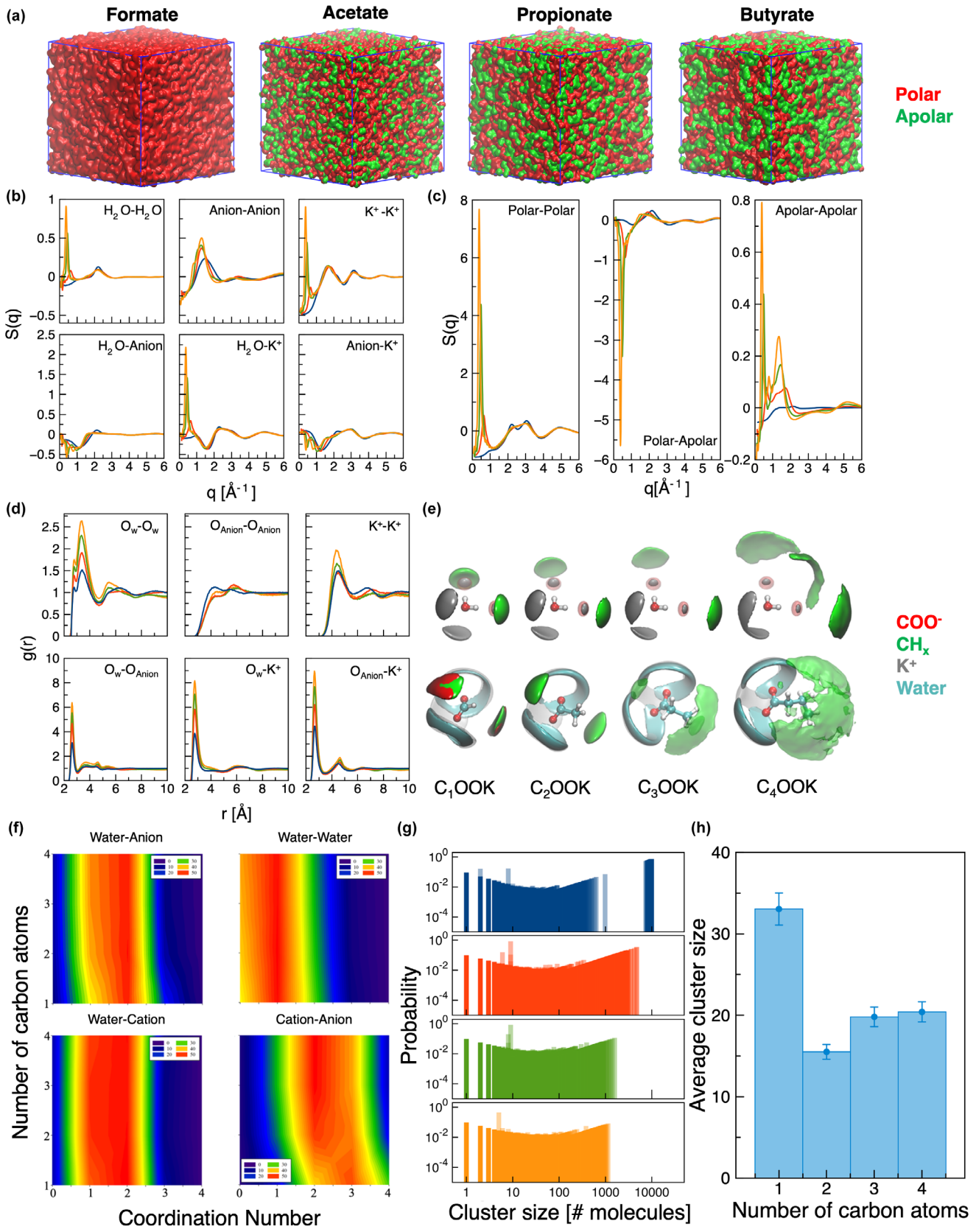

Figure 2. a) Simulation snapshots with water omitted. Polar component (red): K^+ and the carboxylate headgroup. Apolar component (green): anion alkyl tails. b) Species-resolved partial $S(q)$. c) Polarity-resolved partial $S(q)$. d) Radial distribution functions for selected atom pairs. e) Spatial distribution functions for isosurfaces at 1.5× bulk density. f) Coordination number maps. g) Water cluster population distributions. h) Mean cluster size by system. Color code for traces in b, c, d, g: formate blue, acetate red, propionate green, butyrate orange.

between classical small-angle and mid-q structuring in the measurements and why the feature is less coherent than in C_2OOK–C_4OOK. It is thus consistent to interpret the C_1OOK feature as intermediate-range order governed by hydration rather than by a polarity-segregated modulation. Such structural observations place C_1OOK more on the side of conventional salt-in-water solutions rather than water-in-salt. Spatial distribution functions (SDFs, Figure 2e) supply a geometric cross-check that does not rely on absolute scattering amplitude. With water at the origin, SDFs show an increase of K^+ probability density in the first hydration environment as the anion tail grows, accompanied by a decrease of water probability in that same local region, while the carboxylate oxygen environment around water changes little across the series. With the anion as origin, the most pronounced evolution is the growth of aliphatic density around the chain as the tail gets longer, whereas the polar environment near the headgroup remains nearly invariant. Radial Distribution Functions (RDFs, Figure 2d) and coordination numbers (Figure 2f) quantify the near-invariance of first-shell structure, which is crucial for interpreting the SWAXS line-shape evolution. The K^+–O_w first-shell maximum remains near the same distance for all four salts, and the corresponding coordination numbers vary only within statistical uncertainty, consistent with classic hydration benchmarks for simple cations in water-rich environments.[53–55] Water–anion hydrogen bonds populate the same primary-shell distances and angles across the series, in line with typical O···H distances and angular preferences reported for aqueous carboxylates and concentrated aqueous media.[53–55] These invariances show that the SWAXS left shift of $q_{pre\text{-}peak}$ and the modest narrowing from C_2OOK to C_4OOK do not arise from first-shell rearrangement around ions or headgroups; they arise from medium-range polarity modulation that the BT channels identify explicitly. Solvent-accessible surface area (SASA) quantifies the portion of a solute's surface that a spherical solvent probe can touch; operationally, it is the "rolling-sphere" molecular surface introduced by Lee and Richards.[56] SASA is most commonly computed with the Shrake–Rupley point-sampling algorithm, which places a shell of points at one probe radius beyond each van der Waals sphere and counts those not occluded by neighbors.[57] Standard implementations are widely available, for example, FreeSASA, which provides reproducible command-line and library tools for trajectory analysis.[58] In this work, SASA is used as a geometric proxy for water exposure that complements the BT-channel view of internal polarity segregation: SASA reports how much of each anion is accessible to water at any instant, whereas the SWAXS $q_{pre\text{-}peak}$ and the MD BT decomposition report the length scale and sign pattern of concentration fluctuations. Per-anion solvent-accessible surface area, computed with water as the probe solvent and the entire salt as the solute, provides a geometric readout that is independent of scattering amplitudes yet directly comparable across the series. The totals increase from C_1OOK to C_3OOK and then dip for C_4OOK (**Table 2**). From C_1OOK to C_3OOK, the tails are relatively short and remain largely exposed to the polar environment, so the increase in SASA mainly reflects simple growth of hydrophobic surface. For C_4OOK, the additional methylene unit makes tail–tail association significantly more favorable, and the butyrate chains reorganize into thicker, more compact alkyl regions in which a substantial fraction of the tail surface is buried. The net decrease in SASA at C_4OOK therefore reflects cooperative self-shielding of the hydrophobic volume, rather than a reduction in polarity segregation.

Table 2. Solvent-accessible surface area (SASA) calculated for the four different systems.

Anion	SASA (Å^2)
Formate	612.52
Acetate	687.26
Propionate	765.30
Butyrate	720.46

Within the present series, the SASA analysis is consistent with the experimental SWAXS TS-based picture of tail bundling at C_4OOK. As the alkyl chain length increases, the pre-peak full width at half maximum decreases, while ξ/d rises from values close to unity to values characteristic of an underdamped modulation (Table S3, Supporting Information and Figure 1a,d). This evolution implies a more regular compositional modulation and smoother interfaces between polar and apolar regions in the butyrate salt. Combined with the SASA decrease and the MD snapshots, which show a larger fraction of the C_4OOK tail buried in alkyl-rich aggregates, the SWAXS line shape therefore provides an independent signature of enhanced tail self-shielding in that system. Moreover, the rise of SASA from C_1OOK to C_3OOK reflects the larger water-exposed envelope as the tail lengthens. The overall interpretation aligns with the BT-channel pattern for C_2OOK–C_4OOK, where like-polarity correlations rise in phase at $q_{pre\text{-}peak}$ and the cross-polarity channel shows an anti-peak. It also remains compatible with the near-invariance of first-shell hydration metrics across the series, which points to medium-range reorganization rather than primary coordination changes as the origin of the SWAXS left-shift and modest narrowing. In short, a lower total SASA at C_4OOK does not contradict a longer and better-defined modulation length; SASA reports water accessibility, whereas the SAXS $q_{pre\text{-}peak}$ and BT analysis report internal segregation on the nanometer scale. Water network connectivity was quantified by cluster statistics over the production trajectories. The distributions are broad and right-skewed at 20 m for all salts, as expected in dense ionic solutions (Figure 2g, and **Table 3**). The mean cluster size decreases sharply from C_1OOK to C_2OOK and then stabilizes, within uncertainty, for C_3OOK and C_4OOK (Figure 2h).

Table 3. Average water cluster size in the four systems.

Anion	Average number of water molecules in clusters
Formate	33.04 ± 4.67
Acetate	15.51 ± 1.25
Propionate	19.81 ± 1.63
Butyrate	20.41 ± 2.38

The sharp decrease in average water cluster size from C_1OOK to C_2OOK reflects a qualitative change in regime. For C_1OOK, the system behaves as a salt-in-water solution: Water forms extended, almost bulk-like hydrogen-bonded domains, and the topology analysis therefore identifies large, often percolating clusters. In C_2OOK at the same nominal concentration, the additional methylene group on the anion is sufficient to drive a transition to a water-in-salt morphology, in which water is redistributed into K^+-rich channels and pockets separated by alkyl-rich regions. These truncate the water domains resulting in much smaller clusters, even though the overall water content is unchanged. Between C_2OOK and C_4OOK, the total amount of water and the connectivity of the K^+–water network remain similar. Tail bundling in C_4OOK, however, slightly thickens the polar channels and relaxes the curvature of the polar–apolar interface. This allows somewhat larger water sub-domains to form within the percolating K^+–water network, which explains the modest increase in average cluster size from acetate to butyrate without recovering the large, bulk-like clusters seen for C_1OOK. In this sense, the cluster-connectivity measure is the real-space counterpart of the SWAXS pre-peak: Both quantify how the increasing apolar content punctuates and reshapes the polar network on the modulation length d while leaving local hydrogen bonding largely intact. A distinct shoulder appears near $q \approx 1.5$ Å^{-1} (see Figure 1) in the experiment for C_3OOK and C_4OOK. In the model, this feature is reproduced by out-of-phase (minima) cation–anion partial structure factors together with in-phase (maxima) like-charge terms in the BT decomposition (Figure 2b,c), which is the classical signature of local charge alternation on a few-Ångstrom scale.[49] The associated real-space length, roughly 4.2 Å, is characteristic of short-range ordering and is distinct from the longer modulation length d that sets $q_{pre\text{-}peak}$. The coexistence of a low-q polarity-segregated fluctuation and a mid-q charge-alternation feature therefore explains why the measured patterns do not require or display a harmonic at $2{\cdot}q_{pre\text{-}peak}$. The two features arise from different channels and length scales and can vary in intensity independently.[50,59] This is consistent with experimental studies that report prominent charge-alternation signatures in concentrated electrolytes and ionic liquids without higher-order harmonics of the low-q maximum in the same q-range.[39,60,61] Bringing these elements together, the MD observables rationalize the SWAXS pre-peak positions and line shapes across the series. For C_2OOK–C_4OOK, amphiphilic bicontinuity is now demonstrated, not only suggested: a periodic-boundary percolation analysis on the trajectories shows that both the alkyl-rich and the polar domain (water + K^+ plus carboxylate O) form system-spanning clusters in at least two of three axes for at least 80% of frames, with the largest-cluster fraction $\geq$0.80 across the run; the procedure, cutoffs, and full statistics are reported in the Supporting Information. Longer tails increase the apolar volume fraction, consolidate the tail network, and coarsen the polar–apolar modulation, which at fixed composition yields a monotonic shift of $q_{pre\text{-}peak}$ to smaller values and a progressive narrowing of the line shape. Snapshots are consistent with this picture, showing continuous tail domains for C_2OOK–C_4OOK upon water removal, while C_1OOK lacks such connectivity and remains hydration-dominated, as indicated by the polarity-grouped partial factors, SDFs, and coordination trends. The mid-q shoulder near 1.5 Å^{-1} tracks charge alternation and is largely decoupled from the low-q modulation, explaining its evolution without invoking multiple small-angle harmonics. On this basis, we assign a distorted sponge-like (L_3) bicontinuous morphology to C_2OOK–C_4OOK at 20 m, and a non-bicontinuous, hydration-dominated structure to C_1OOK.

4. Electrochemical Properties

We evaluated electrochemical stability and ionic transport of the 20 m solutions to connect the distorted-L_3 bicontinuous structure resolved by SWAXS/MD with performance metrics. Linear sweep voltammetry in three-electrode cell configuration yields the apparent stability ranking C_2OOK > C_3OOK > C_4OOK > C_1OOK. The window expands sharply from C_1OOK to C_2OOK and then changes modestly with further tail growth, with both anodic and cathodic limits shifting from C_1OOK to C_2OOK and a predominantly cathodic gain from C_2OOK to C_4OOK (**Figure 3**). This hierarchy is consistent with the canonical WiSE view that reduced water activity and interfacial water depletion suppress hydrogen and oxygen evolution, thereby widening the apparent aqueous ESW beyond dilute-solution expectations.[13,16,19,20] Theory and simulation further indicate that, in the concentrated regime, the electrical double layer becomes depleted of contiguous water. The interfacial structure and solvation thermodynamics, not bulk pH alone, whose meaning is questionable at these concentrations,[22] set the onsets.[19,20] The MD results help in rationalizing the ESW trend. Longer tails magnify polar–apolar segregation, thin and truncate water connectivity, and relocate water away from anion-rich regions on the $q_{pre\text{-}peak}$ length scale. This explains the substantial ESW increase from C_1OOK to C_2OOK and the smaller incremental gains thereafter. The link is made quantitative by water cluster statistics at 20 m (Figure 2g,h). The widest ESW coincides with the smallest average water cluster size (C_2OOK), whereas the narrowest ESW coincides with the largest clusters (C_1OOK), with the other systems in between. Within the C_xOOK family, smaller clusters indicate that water has been redistributed from extended, bulk-like domains into confined K^+ rich channels. This redistribution lowers the effective water activity and is consistent with a more difficult stabilization of H^+ and OH^- at reactive interfaces, which are the main responsible for the stability of the electrolyte. This is consistent with the general view from water-in-salt electrolytes that ESW broadening is governed by water activity and by the local solvation thermodynamics of H^+, OH^-, and SEI-forming ions rather than by cluster size alone.[14,62] In other systems, such as LiTFSI-based WiSE, large ionic clusters can coexist with wide ESW when cluster growth is accompanied by strong binding of water to Li^+ and a marked decrease in water activity. Our data therefore support an inverse ESW–cluster size correlation within this homologous series at 20 m, while we identify the more general design message as the need to reduce water activity in the relevant interfacial environment. This interpretation is consistent with recent work that disentangles structural descriptors from underlying thermodynamics. McEldrew et al.[52] showed for LiTFSI water-in-salt electrolytes that the broadening of the electrochemical stability window at high salt concentration tracks a strong decrease in water activity as water molecules become bound in the cation solvation shell, and that growing ionic clusters can coexist with wide ESW when they accompany this drop-in activity. Sui et al.[63] demonstrated across a broad set of aqueous electrolytes that ESW shifts correlate with ionic potential and with the solvation energies of proton and hydroxide, rather than with any single structural metric, and that bulky, low charge density ions create chemical environments that frustrate proton and hydroxide solvation and render water more redox inert. Our C_xOOK series therefore provides a specific example in which smaller water clusters correlate with a wider ESW because they reflect stronger water confinement and a reduction of effective water activity. The broader design lesson, consistent with the literature, is that ESW is ultimately controlled by

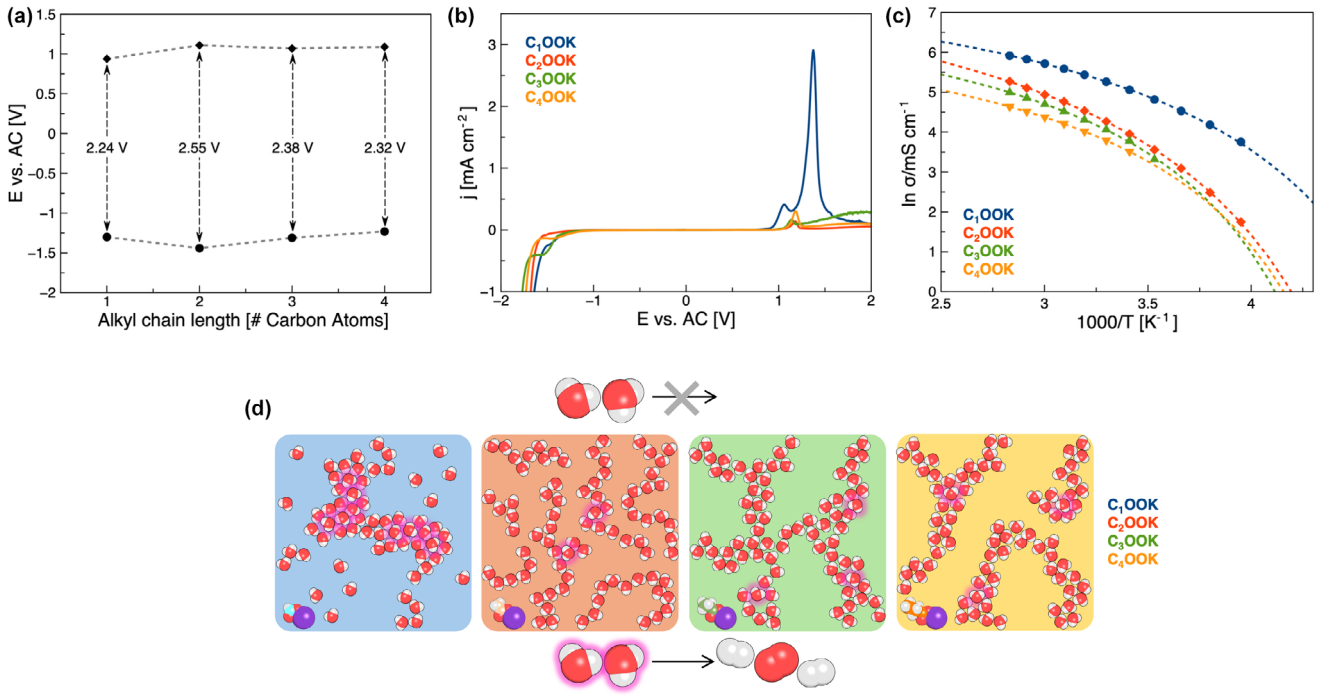

Figure 3. Chain length-dependent electrochemical stability. a) Electrochemical stability split into cathodic and anodic contribution. b) Linear sweep voltammetry recorded at 0.1 mV s^{-1}. c) Arrhenius plot for the conductivity. Symbols are for experimental values (C_1OOK circles, C_2OOK diamonds, C_3OOK triangles, C_4OOK inverted triangles) while dashed lines represent the VTF fittings. d) Schematic summary of the key finding: Each colored box represents a different water-in-salt electrolyte, with water molecules arranged to qualitatively reflect the water cluster size distribution. Water molecules with purple halos indicate the subset classified as "reactive" water, used here as a qualitative proxy for water activity (more halos correspond to higher effective water activity). Color code for traces in b, c, and for background color in d: formate blue, acetate red, propionate green, butyrate orange.

water activity and local solvation thermodynamics, with clustering acting only as an indirect but reliable and easily accessed proxy. Temperature-dependent conductivity was also measured from −20 to 80 °C for the solution of all salts, with two exceptions due to phase behavior: For C_3OOK visible precipitation occurred below 10 °C and for C_4OOK below 20 °C, so data at lower temperatures were omitted for those systems. Conductivity increases monotonically with temperature within the accessible ranges (Figure 3). The Vogel–Tammann–Fulcher (VTF) description,

$$\sigma = \sigma_0 \, e^{-B/R(T-T_0)}, \quad (4)$$

captures the non-Arrhenius character typical of crowded ionic media. Here B is a pseudo-activation parameter and T_0 the Vogel temperature or temperature of zero configurational entropy (Table 4, Figure 3).

The VTF description is statistically superior for all salts, consistent with the extensive literature on ionic liquids and highly concentrated electrolytes where conductivity commonly follows VTF and fragility tracks mesoscale structure. The VTF parameters reveal two robust trends. First, the Vogel temperature increases from C_1OOK to C_3OOK and then decreases slightly for C_4OOK. The initial rise is consistent with transport that becomes progressively coupled to a slower, more structured matrix as the polar–apolar modulation coarsens. The small reduction for C_4OOK is compatible with tail bundling that partially relieves interfacial curvature and water-path tortuosity, a behavior also echoed by SASA inversion and by the MD snapshots, without altering the underlying bi-continuity. Second, the VTF pre-factor σ_0 decreases across the series after acetate. Together, higher T_0 and lower σ_0 with increasing amphiphilicity indicate stronger dynamical coupling to the nano-segregated matrix, fully consistent with the literature on ionic liquids and highly concentrated electrolytes where conductivity commonly follows VTF behavior and fragility tracks mesoscale structure. A structure–transport correlation emerges at fixed temperature. At 20 °C, σ decreases as the SWAXS-derived modulation length d increases from C_1OOK through the longer-tail salts. C_1OOK exhibits the smallest d and the highest σ; C_2OOK–C_4OOK show larger d, lower σ, and stronger temperature sensitivity. In a bicontinuous medium where water-rich corridors carry a large fraction of the current, coarsening of the polar–apolar modulation reduces pathway multiplicity and increases tortuosity, which strengthens the temperature dependence of long-range motion. This negative d–σ correlation is consistent with the growth of T_0 from C_1OOK to C_3OOK, with the slight reduction at C_4OOK

Table 4. VTF fitting parameters and fitting goodness metrics for the temperature-dependent conductivity. More metrics in Table S8, Supporting Information.

	σ_0 [mS cm^{-1}]	|B| [J mol^{-1}]	T_0 [K]	R^2	RMSE
C_1OOK	1909 ± 95	2358 ± 106	179 ± 2.8	0.99985	1.56616
C_2OOK	1926 ± 177	3152 ± 195	188 ± 3.9	0.99979	1.03079
C_3OOK	1008 ± 128	2440 ± 255	200 ± 6.1	0.99967	0.90079
C_4OOK	630 ± 10	2357 ± 36	196 ± 0.9	0.99999	0.06131

explained by tail bundling, and with MD evidence for truncated water clusters and enhanced mid-q charge alternation for longer tails. It also accords with WiSE reports that conductivity often decreases deeper into the water-poor regime, while ESW increases as water activity falls.[13,64] While the scattering–transport relations are clear at the level of positions and T_0, a one-to-one mapping between any single structural metric and conductivity amplitude is not expected. Conductivity reflects a convolution of concentration–concentration fluctuations, charge–charge correlations, ion pairing, and viscosity. In crowded ionic environments, transport may partially decouple from structural relaxation, a behavior captured by Walden and VTF analyses in ionic liquids and concentrated electrolytes.[33,65–67] Within these known limits, the present series is internally consistent: Smaller water clusters accompany larger ESW; larger d and higher T_0 accompany lower σ at a given T. Thus, stability and transport are controlled by the same medium-range segregation quantified by SWAXS and MD. To further connect structure and transport, we measured the viscosities of C_1OOK and C_2OOK using a simple drop viscometer with water as calibration fluid. From the drop times (Table S10, Supporting Information) and the known kinematic viscosity of water, we obtained kinematic viscosities of 1.53 ± 0.07 cSt for C_1OOK and 7.19 ± 0.23 cSt for C_2OOK. Thus, under our conditions, C_2OOK is about a factor of 4.7 more viscous than C_1OOK. Ionic conductivity in concentrated electrolytes is strongly influenced by viscous drag on the charge carriers, providing an explanation for the highest conductivity of C_1OOK relative to C_2OOK, despite the larger water clusters in C_1OOK. Both solutions were measured in the same instrument and geometry, so any modest non-Newtonian behavior should affect them similarly and cannot invert this strong viscosity contrast.

5. Conclusions

At fixed composition (20 m), fluorine-free, water-in-natural-salt electrolytes based on potassium carboxylates exhibit a clear, composition tunable medium-range order that links directly to performance. Small-angle X-ray scattering resolves a pre-peak that shifts to lower q with increasing alkyl tail length, mapping to a larger real-space modulation length ($d = 2\pi/q_{\text{pre-peak}}$). The absence of a detectable feature at $2{\cdot}q_{\text{pre-peak}}$, together with the development of a mid-q shoulder near ≈ 1.5 Å^{-1} for the longer tails, supports a distorted L_3, sponge-like bicontinuous morphology rather than lamellae. Molecular dynamics reproduces the SWAXS positions and assigns the pre-peak to concentration–concentration fluctuations: polar domains enriched in water and K^+ co-fluctuate in phase, anticorrelated with anion-centered and apolar domains at the same length scale. Spatial distribution functions, hydrogen bond statistics, and water cluster populations indicate that water is predominantly engaged at polar–apolar interfaces and that extended bulk-like reservoirs are disfavored beyond C_1OOK. These structural signatures rationalize the trends in electrochemical response and transport. The overall assignment is compatible with SWAXS comparisons with molecular amphiphiles, where pre-peak positions reflect domain spacing rather than intensity, and to ionic liquids, where sponge-like bi-continuity is the accepted interpretation of low-q features. Within this series, the electrochemical stability window widens sharply from C_1OOK to C_2OOK and changes only modestly from C_2OOK to C_4OOK, whereas conductivity decreases monotonically with increasing tail length. In parallel, the average size of water clusters obtained from molecular dynamics decreases strongly from formate to acetate and then varies only weakly for the longer tails. Taken together, these observations identify an inverse correlation between ESW and water cluster size: Salts that truncate bulk-like water connectivity exhibit wider stability windows, while more hydrophilic compositions with larger water clusters retain higher conductivity. The key finding of the optimal balance between water segregation and water clustering is schematized in Figure 3d. The combination of structure, stability, and transport identifies a clear optimum in the present series. At 20 m, C_2OOK is the shortest anion that already produces a water-in-natural-salt morphology, a pronounced ESW gain, and significantly smaller water clusters, without incurring the larger hydrophobic volume and mobility penalty expected for longer chains. In this sense, acetate marks a practical sweet spot between stability and transport at fixed composition. More generally, the C_xOOK series shows that structural changes can be used as design handles to balance electrochemical stability and ionic mobility in fluorine-free aqueous electrolytes.

6. Experimental Section

Detailed information related to the synthesis of active electrodes, physicochemical characterization, and electrochemical evaluation of bifunctional electrodes towards UOR and supercapacitor application is provided in Supporting Information.

Acknowledgements

A.D.G. and L.H. contributed equally to this work. L.H., J.H., R.K.H., and A.V. sincerely acknowledge the BMFT (Bundesministerium für Forschung, Technologie und Raumfahrt) for funding this work within the project "NASS" (03XP0490A). SP acknowledges the Helmholtz Association's basic funding. The authors gratefully acknowledge Prof. Matteo Bonomo for the viscosity measurements and the fruitful discussion. A.M., A.D.G., and L.G. dedicate a special acknowledgment to the late Prof. Nicolae Viorel Pavel, whose expertise, encouragement, and early contributions to the SAXS/WAXS characterization were essential to the realization of this research. His memory continues to inspire our work. Open access publishing facilitated by Politecnico di Milano, as part of the Wiley - CRUI-CARE agreement.

Conflict of Interest

The authors declare no conflict of interest.

Supporting Information

Supporting Information is available from the Wiley Online Library or from the author.

Keywords

batteries, electrochemistry, electrolytes, environmental materials, molecular dynamics

Received: November 6, 2025
Revised: December 17, 2025
Published online: February 15, 2026

[1] J.-M. Tarascon, M. Armand, *Nature* **2001**, *414*, 359.
[2] J. B. Goodenough, K.-S. Park, *J. Am. Chem. Soc.* **2013**, *135*, 1167.
[3] N. Nitta, F. Wu, J. T. Lee, G. Yushin, *Mater. Today* **2015**, *18*, 252.

[4] K. Xu, *Chem. Rev.* **2004**, *104*, 4303.
[5] Y. Chen, Y. Kang, Y. Zhao, L. Wang, J. Liu, Y. Li, Z. Liang, X. He, X. Li, N. Tavajohi, B. Li, *J. Energy Chem.* **2021**, *59*, 83.
[6] X. Feng, M. Ouyang, X. Liu, L. Lu, Y. Xia, X. He, *Energy Storage Mater.* **2018**, *10*, 246.
[7] M. S. Whittingham, *Chem. Rev.* **2020**, *120*, 6328.
[8] J.-Y. Hwang, S.-T. Myung, Y.-K. Sun, *Chem. Soc. Rev.* **2017**, *46*, 3529.
[9] C. Vaalma, D. Buchholz, S. Passerini, *Curr. Opin. Electrochem.* **2018**, *9*, 41.
[10] P. Canepa, G. Sai Gautam, D. C. Hannah, R. Malik, M. Liu, K. G. Gallagher, K. A. Persson, G. Ceder, *Chem. Rev.* **2017**, *117*, 4287.
[11] M. E. Arroyo-de Dompablo, A. Ponrouch, P. Johansson, M. R. Palacín, *Chem. Rev.* **2020**, *120*, 6331.
[12] W. Du, E. H. Ang, Y. Yang, Y. Zhang, M. Ye, C. C. Li, *Energy Environ. Sci.* **2020**, *13*, 3330.
[13] L. Suo, O. Borodin, T. Gao, M. Olguin, J. Ho, X. Fan, C. Luo, C. Wang, K. Xu, *Science* **2015**, *350*, 938.
[14] L. Suo, O. Borodin, W. Sun, X. Fan, C. Yang, F. Wang, T. Gao, Z. Ma, M. Schroeder, A. von Cresce, S. M. Russell, M. Armand, A. Angell, K. Xu, C. Wang, *Angew. Chem. Int. Ed.* **2016**, *55*, 7136.
[15] Y. Yamada, K. Usui, K. Sodeyama, S. Ko, Y. Tateyama, A. Yamada, *Nat. Energy* **2016**, *1*, 16129.
[16] N. Dubouis, P. Lemaire, B. Mirvaux, E. Salager, M. Deschamps, A. Grimaud, *Energy Environ. Sci.* **2018**, *11*, 3491.
[17] O. Borodin, J. Self, K. A. Persson, C. Wang, K. Xu, *Joule* **2020**, *4*, 69.
[18] C.-Y. Li, M. Chen, S. Liu, X. Lu, J. Meng, J. Yan, H. D. Abruña, G. Feng, T. Lian, *Nat. Commun.* **2022**, *13*, 5330.
[19] J. Vatamanu, O. Borodin, *J. Phys. Chem. Lett.* **2017**, *8*, 4362.
[20] M. McEldrew, Z. A. H. Goodwin, A. A. Kornyshev, M. Z. Bazant, *J. Phys. Chem. Lett.* **2018**, *9*, 5840.
[21] J. Han, A. Mariani, M. Zarrabeitia, Z. Jusys, R. J. Behm, A. Varzi, S. Passerini, *Small* **2022**, *18*, 2201563.
[22] J. Han, A. Mariani, S. Passerini, A. Varzi, *Energy Environ. Sci.* **2023**, *16*, 1480.
[23] S. Chen, R. Lan, J. Humphreys, S. Tao, *Energy Storage Mater.* **2020**, *28*, 205.
[24] S. Khalid, N. Pianta, S. Bonizzoni, C. Ferrara, R. Lorenzi, A. Paleari, P. Johansson, P. Mustarelli, R. Ruffo, *J. Phys. Chem. C* **2023**, *127*, 9823.
[25] H. Zhang, X. Liu, H. Li, I. Hasa, S. Passerini, *Angew. Chem. Int. Ed.* **2021**, *60*, 598.
[26] R.-S. Kühnel, D. Reber, A. Remhof, R. Figi, D. Bleiner, C. Battaglia, *Chem. Commun.* **2016**, *52*, 10435.
[27] A. Triolo, O. Russina, H.-J. Bleif, E. Di Cola, *J. Phys. Chem. B* **2007**, *111*, 4641.
[28] A. Mariani, A. Innocenti, A. Varzi, S. Passerini, *Phys. Chem. Chem. Phys.* **2021**, *23*, 20282.
[29] M. Požar, J. Bolle, C. Sternemann, A. Perera, *J. Phys. Chem. B* **2020**, *124*, 8358.
[30] K. R. Harris, *J. Phys. Chem. B* **2019**, *123*, 7014.
[31] C. Schreiner, S. Zugmann, R. Hartl, H. J. Gores, *J. Chem. Eng. Data* **2010**, *55*, 1784.
[32] X. Liu, S.-C. Lee, S. Seifert, L. He, C. Do, R. E. Winans, G. Kwon, Y. Zhang, T. Li, *Chem. Mater.* **2023**, *35*, 2088.
[33] A. Mariani, M. Bonomo, X. Gao, B. Centrella, A. Nucara, R. Buscaino, A. Barge, N. Barbero, L. Gontrani, S. Passerini, *J. Mol. Liq.* **2021**, *324*, 115069.
[34] J. Han, M. Zarrabeitia, A. Mariani, Z. Jusys, M. Hekmatfar, H. Zhang, D. Geiger, U. Kaiser, R. J. Behm, A. Varzi, S. Passerini, *Nano Energy* **2020**, *77*, 105176.
[35] J. Han, A. Mariani, A. Varzi, S. Passerini, *J. Power Sources* **2021**, *485*, 229329.
[36] A. Mariani, P. Ballirano, F. Angiolari, R. Caminiti, L. Gontrani, *ChemPhysChem* **2016**, *17*, 3023.
[37] J. N. A. Canongia Lopes, A. A. H. Pádua, *J. Phys. Chem. B* **2006**, *110*, 3330.
[38] A. Mariani, R. Caminiti, M. Campetella, L. Gontrani, *Phys. Chem. Chem. Phys.* **2016**, *18*, 2297.
[39] R. Hayes, S. Imberti, G. G. Warr, R. Atkin, *Phys. Chem. Chem. Phys.* **2011**, *13*, 3237.
[40] L. Gontrani, R. Caminiti, U. Salma, M. Campetella, *Chem. Phys. Lett.* **2017**, *684*, 304.
[41] D. I. Svergun, M. H. J. Koch, *Rep. Prog. Phys.* **2003**, *66*, 1735.
[42] C. M. Jeffries, J. Ilavsky, A. Martel, S. Hinrichs, A. Meyer, J. S. Pedersen, A. V. Sokolova, D. I. Svergun, *Nat. Rev. Methods Primers* **2021**, *1*, 70.
[43] C. Tanford, *J. Phys. Chem.* **1972**, *76*, 3020.
[44] C. Tanford, *J. Phys. Chem.* **1974**, *78*, 2469.
[45] K.-V. Schubert, R. Strey, S. R. Kline, E. W. Kaler, *J. Chem. Phys.* **1994**, *101*, 5343.
[46] M. Teubner, R. Strey, *J. Chem. Phys.* **1987**, *87*, 3195.
[47] P. Juhás, T. Davis, C. L. Farrow, S. J. L. Billinge, *J. Appl. Crystallogr.* **2013**, *46*, 560.
[48] A. B. Bhatia, D. E. Thornton, *Phys. Rev. B* **1970**, *2*, 3004.
[49] J. C. Araque, J. J. Hettige, C. J. Margulis, *J. Phys. Chem. B* **2015**, *119*, 12727.
[50] R. Ogbodo, W. V. Karunaratne, G. R. Acharya, M. S. Emerson, M. Mughal, H. M. Yuen, N. Zmich, S. Nembhard, F. Wang, H. Shirota, S. I. Lall-Ramnarine, E. W. Castner, J. F. Wishart, A. J. Nieuwkoop, C. J. Margulis, *J. Phys. Chem. B* **2023**, *127*, 6342.
[51] H. K. Kashyap, J. J. Hettige, H. V. R. Annapureddy, C. J. Margulis, *Chem. Commun.* **2012**, *48*, 5103.
[52] M. McEldrew, Z. A. H. Goodwin, S. Bi, A. A. Kornyshev, M. Z. Bazant, *J. Electrochem. Soc.* **2021**, *168*, 050514.
[53] H. Ohtaki, T. Radnai, *Chem. Rev.* **1993**, *93*, 1157.
[54] X. Zhang, R. Kumar, D. G. Kuroda, *J. Chem. Phys.* **2018**, *148*, 094506.
[55] J. Mähler, I. Persson, *Inorg. Chem.* **2012**, *51*, 425.
[56] B. Lee, F. M. Richards, *J. Mol. Biol.* **1971**, *55*, 379.
[57] A. Shrake, J. A. Rupley, *J. Mol. Biol.* **1973**, *79*, 351.
[58] S. Mitternacht, *F1000Res* **2016**, *5*, 189.
[59] T. S. Groves, C. S. Perez-Martinez, R. Lhermerout, S. Perkin, *J. Phys. Chem. Lett.* **2021**, *12*, 1702.
[60] R. Atkin, G. G. Warr, in *ACS Symp. Ser.*, American Chemical Society, Washington DC **2010**, pp. 317–333.
[61] R. Hayes, G. G. Warr, R. Atkin, *Chem. Rev.* **2015**, *115*, 6357.
[62] D. Gomez Vazquez, J. Ingenmey, K. Trapp, D. Ciliak, M. Salanne, M. R. Lukatskaya, *J. Am. Chem. Soc.* **2025**, *147*, 35953.
[63] Y. Sui, A. M. Scida, B. Li, C. Chen, Y. Fu, Y. Fang, P. A. Greaney, T. M. Osborn Popp, D. Jiang, C. Fang, X. Ji, *Angew. Chem. Int. Ed.* **2024**, *63*, e202401555.
[64] D. A. C. Da Silva, C. M. J. Pinzón, A. Messias, E. E. Fileti, A. Pascon, D. V. Franco, L. M. Da Silva, H. G. Zanin, *Mater. Adv.* **2022**, *3*, 611.
[65] J. Vila, P. Ginés, J. M. Pico, C. Franjo, E. Jiménez, L. M. Varela, O. Cabeza, *Fluid Phase Equilib.* **2006**, *242*, 141.
[66] J. Leys, M. Wübbenhorst, C. P. Menon, R. Rajesh, J. Thoen, C. Glorieux, P. Nockemann, B. Thijs, K. Binnemans, S. Longuemart, *J. Chem. Phys.* **2008**, *128*, 064509.
[67] H. M. Schütz, S. Nejrotti, H. Adenusi, A. Mariani, E. Bodo, M. Bonomo, A. Innocenti, C. Barolo, X. Gao, S. Passerini, *J. Mater. Chem. A* **2024**, *12*, 18412.